Physics Extended Essay

Title: An investigation into the effect of hopper wall inclination angle on the flow rate of sand through a wedge-shaped hopper.

Research Question: How does hopper angle affect the flow rate of sand through a wedge-shaped hopper with a square aperture?

3847 words

Table of Contents

1.1 Introduction and Rationale

Hoppers are large structures often used in industry to collect and transfer granular material, such as sand, from one bin to another. Typically used with other mechanical parts like conveyors as part of a larger system, they have numerous applications in fields such as manufacturing and agriculture. Hoppers serve to streamline the manufacturing process; they must be able to work seamlessly together with other components for the efficient completion of the process. One of the most important aspects of hopper design that must be considered is its ability to tailor the flow rate of the granular material to appropriately suit its application; having a too slow flow rate could cause particles to jam and accumulate at the hopper, resulting in inefficiency of downstream processes. On the other hand, the system may not be able to accommodate too great a flow rate, carrying a high risk of mechanical failure if particle flow becomes unmanageable.

Hopper geometry is greatly varied, depending on their necessary applications, with the two main types being conical and wedge-shaped. Conical hoppers have traditionally been the focus of much study as they are widely used for their simple shape, generally allowing for lower costs of design and manufacturing (Guo, 2023). However, wedge-shaped hoppers have been adopted due for efficiency; wedge-shaped hoppers are capable of exhibiting mass flow at less steep hopper angles (Jenike, 2964), allowing for a shorter hopper of the same capacity to be used. Despite this, there has been a lack of study on wedge-shaped hoppers. Beverloo's equation is the most commonly cited equation governing flow rate, but it was formulated based on conical hoppers. The wedge-shaped hopper's hydraulic diameter can be used as an equivalent conversion, but most of the work validating the equation (Wiacek, 2023) has only been done with a focus on conical hoppers.

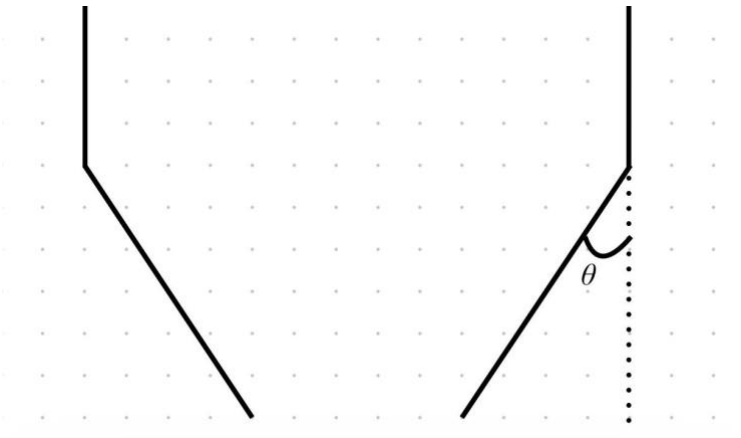

Figure 1: Definition of hopper angle

The angle of wall inclination of wedge-shaped hoppers, henceforth hopper angle as seen in Figure 1, is one of the determinants of particle flow pattern, and thus rate, as elaborated on later. Generally, mass flow is preferred for most applications in industry as it allows for faster flow, avoids particle jamming and minimises stagnation areas. Although a small hopper angle guarantees mass flow, it also necessitates a taller hopper to achieve a functional storage capacity, which may not be feasible due to its spatial requirement. Therefore, determining the critical hopper angle for which mass flow predominates at as large an angle as possible is an important goal of hopper design. Taking into consideration the many industrial applications of wedge-shaped hoppers, the research question of this investigation is as follows: **how does hopper angle affect the flow rate of sand through a wedge-shaped hopper with a square aperture?**

2.1 Literature Review

2.1.1 Beverloo Equation

The empirically derived Beverloo equation (Beverloo, 1961) is currently the most commonly used approximation for the flow rate of coarse particles discharging through an outlet, and is of the form:

$$W = C\rho_b\sqrt{g}(D - kd_p)^{\frac{5}{2}}$$

Where W is the rate of discharge, C is the discharge coefficient, ρ_b is the bulk density of the material, D is the aperture width of the orifice, k is the grain shape coefficient, and d_p is the diameter of the grain. However, the drawback of the Beverloo equation is its inability to predict flow rate based on hopper angle; in particular, the discharge coefficient C must be experimentally determined for the local conditions and accounts for changes in parameters including hopper geometry and material. Additionally, it has been found that the Beverloo equation is only valid for hoppers of sufficiently large aperture sizes. (Wiacek, 2023) The Beverloo equation is thus insufficient for the investigation of the relationship between hopper incline angle and flow rate, on a relatively small scale.

2.1.2 Types of Flow

There are two types of flow describing the discharge of granular material through hoppers. Mass flow occurs in hoppers with a steeper angle of inclination, wherein all particles are continuously moving and those at the bottom-most layer of the hopper flows out first (Maraveas, 2020); in other words, particles follow a ‘first-in, first-out’ pattern. Mass flow is generally preferred for its faster flow rate, occurring at smaller hopper angles.

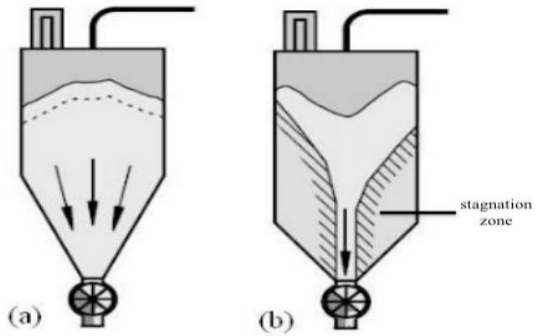

Figure 2: Comparison of mass flow (a) and funnel flow (b). Image taken from external source (Maraveas, 2020), annotated by author.

Funnel flow occurs at less steep angles of hopper inclination. The particles that were filled at the beginning remain along the hopper walls as a result of the gradual hopper angle and friction between the hopper walls and the particles, while a burrowing effect is produced in which particles flow out through a column formed in the middle of the hopper's cross-section (Maraveas, 2020). Once the central particles have flowed out, those on the sides flow through the tunnel; in other words, the particles follow a 'first-in, last-out' pattern. This causes an increased likelihood of formation of so-called 'stagnation areas' at the bottom of the hopper, consisting of particles from the bottom layers which remain stationary.

The critical hopper angle for which mass flow occurs can be varied by a number of factors, such as the hopper and particle materials, which affect wall friction. Since the critical angle is highly dependent on wall friction angle (Jenike, 1964), is in turn dependent on local conditions affecting friction between the hopper walls and the particles, it is not possible to theoretically determine the critical angle for a hopper without in-depth information on the properties of both the particles and hopper material.

The movement of particles undergoing funnel flow is governed by the formation and collapse of arches at the mouth of the hopper (Oldal, 2011), whereby particles slow down and momentarily stop before leaving the arch and entering free-fall. Tang et al. (2022) describes arch formation on a mechanical level and confirm the arch formation hypothesis via the discrete element simulation method, where the instantaneous velocities and accelerations of particles could be quantitatively predicted.

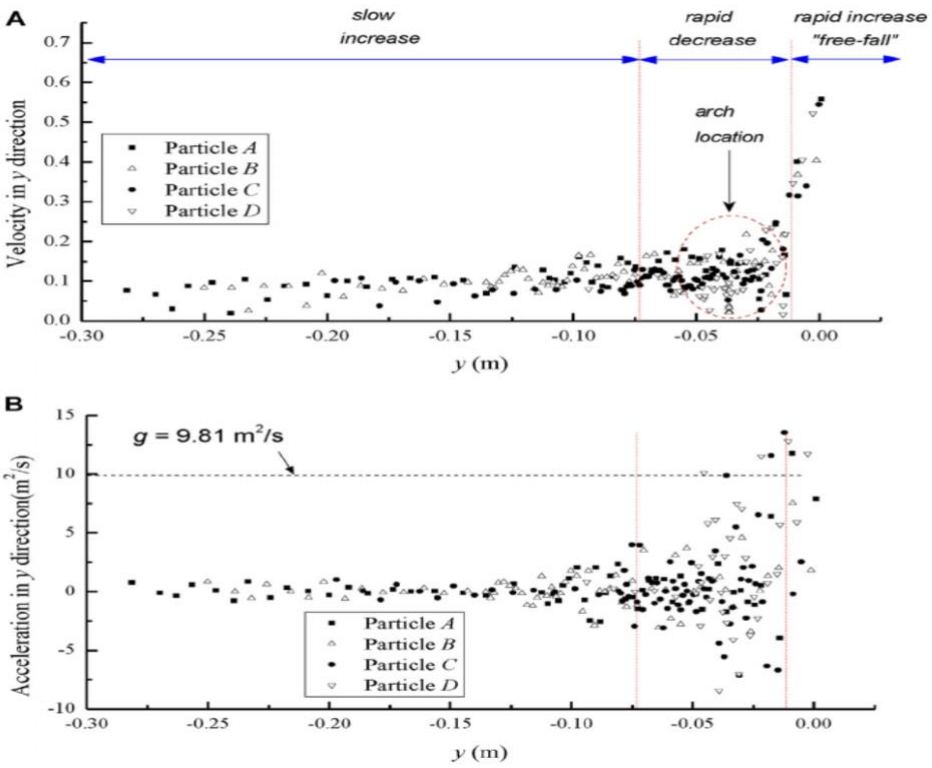

Figure 3: DEM simulation results confirming the arch formation mechanism of funnel flow.

(Tang, 2022)

3.1 Derivation and Hypothesis

As a result of the two different types of particle movement experienced by particles, two different derivations are necessary to observe a relationship between hopper angle and discharge rate.

3.1.1 Deriving Discharge Rate: Mass Flow

The method used by Camila (2018) for predicting mass flow discharge rate from a force balance model is adapted to suit symmetrical grains like sand, rather than elongated seeds.

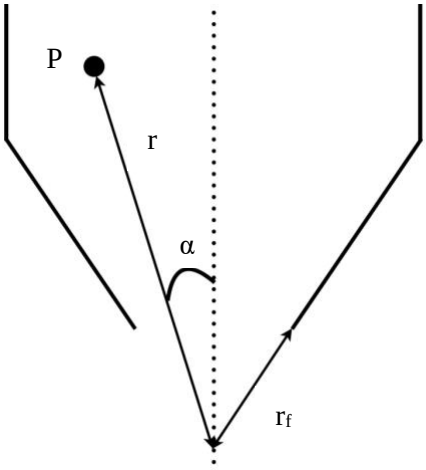

Figure 4: Visualisation of particle during mass flow

Each particle undergoing mass flow is accelerated toward the vertex at the bottom of the hopper. For a smooth hopper, wall friction is assumed to be negligible. As pictured in Figure 4, selecting a random particle P in the hopper with a velocity *v* and distance *r* from the vertex such that an infinitesimally small increase in velocity *dv* is accompanied by an infinitesimally small decrease in distance *dr*,

$$vr = (v + dv)(r - dr)$$

$$vr = vr - vdr + rdv - dvdr$$

$$\frac{dv}{dr} = \frac{v + dv}{r}$$

$$\frac{dv}{dr} \approx \frac{v}{r}$$

Since the velocity v is given by the change in distance r per unit time,

$$v = \frac{dr}{dt}$$

$$dt = \frac{dr}{v}$$

$$a = \frac{dv}{dt}$$

$$a = \frac{vdv}{dr}$$

$$a = \frac{v^2}{r}$$

The force providing this acceleration is given by the component of the particle's weight in the direction of the vertex. If the particle's position subtends an angle α from the vertical axis through the vertex,

$$\frac{mv_f^2}{r_f} = mgcos\alpha$$

$$v_f = \sqrt{gr_f cos\alpha}$$

Where velocity is taken to be positive toward the vertex. The distance from the mouth of the hopper to the vertex, r_f is given by:

$$r_f = \frac{D}{2sin\theta}$$

Where D is the aperture width and θ is the hopper inclination angle. The velocity of the particle at the edge of the hopper mouth is thus given by:

$$v_f = \sqrt{\frac{gDcos\alpha}{2sin\theta}}$$

The vertical component of the velocity of the particle is given by:

$$v = \sqrt{\frac{gDcos\alpha}{2sin\theta}}cos\alpha$$

To find the average velocity of the particles across the width, this is integrated and then divided by the width D, noting that $cos\alpha$ is the only x-dependent variable, with x as the horizontal displacement across the aperture, with the origin at the middle of the aperture:

$$v_{ave} = (\frac{1}{D})(\sqrt{\frac{gD}{2sin\theta}}) \int_{-\frac{D}{2}}^{\frac{D}{2}} cos^{\frac{3}{2}}\alpha \, dx$$

For mass flow to occur, α must be sufficiently small, $\alpha \approx 0$. Thus, cosα can be approximated as 1:

$$v_{ave} = (\frac{1}{D})(\sqrt{\frac{gD}{2sin\theta}}) \int_{-\frac{D}{2}}^{\frac{D}{2}} 1 \, dx$$

$$v_{ave} = (\frac{1}{D})(\sqrt{\frac{gD}{2sin\theta}})(\frac{D}{2} + \frac{D}{2})$$

$$v_{ave} = \sqrt{\frac{gD}{2sin\theta}}$$

The flow rate can then be found by multiplying the average velocity across the width by the area of the square aperture and the bulk density ρ of the material:

$$W_{mass\ flow} = \rho D^2 \sqrt{\frac{gD}{2sin\theta}} \qquad \text{-----(1)}$$

3.1.2 Deriving Discharge Rate: Funnel Flow

To formulate a prediction of flow rate during the funnel flow phase, a similar technique to that used by Oldal (2011) and Camila (2018) is adopted. When the hopper inclination angle becomes sufficiently steep, funnel flow dominates over mass flow. Flow rate is then dependent on the momentary formation and continuous collapse of self-supported arches over the aperture (Oldal, 2011). Each particle is momentarily at rest while the arch is stable, and only falls upon the collapse of the arch. The velocity of each particle at its exit from the hopper is therefore only gained upon its fall from its height in the arch above the aperture. Since it has been found that the arch is parabolic (Nedderman, 1982), its shape can be modelled as:

$$a(x) = h[1 - (\frac{2x}{D})^2]$$

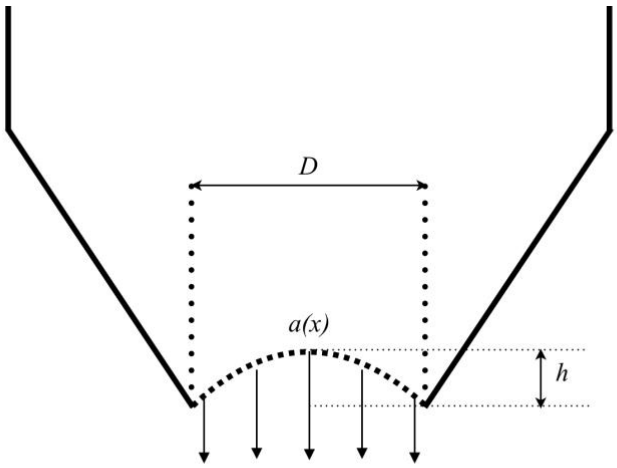

Figure 5: Visualisation of funnel flow arch

Such that h represents the height of the arch and D is the aperture width. Assuming the particles are momentarily at rest, the velocity of a particle exiting the hopper can then be given as:

$$v = \sqrt{2gh[1 - (\frac{2x}{D})^2]}$$

However, the height of the arch formed is not easily quantifiable. Instead, as in Oldal (2011), δ, arch shape coefficient, is introduced as the ratio of *h* to *D*, giving:

$$v = \sqrt{2g\delta D[1 - \frac{4x^2}{D^2}]}$$

Delta characterises the shape of the arch and is primarily dependent on the geometry of individual grains and the flowing material's cohesive properties. Since the only granular material used in this investigation is sand, δ is approximately constant. Integrating and dividing by *D* to find the average velocity per particle along the aperture,

$$v_{ave} = \frac{\sqrt{2g\delta D}}{D} \int_{-\frac{D}{2}}^{\frac{D}{2}} \sqrt{1 - \frac{4x^2}{D^2}}\, dx$$

$$v_{ave} = \frac{\pi D}{4}\sqrt{\frac{2g\delta}{D}}$$

The flow rate is found by multiplying the average velocity across the width by the area of the square aperture and the material's bulk density:

$$W_{funnel\ flow} = \frac{\pi D^3 \rho}{4}\sqrt{\frac{2g\delta}{D}} \qquad \text{-----(2)}$$

3.2.1 Hypothesis

Although these models are simplified and do not consider resistive forces such as air drag and friction between particles, they are sufficient for demonstrating the differences between mass and funnel flow. It is shown that:

$$W_{mass\ flow} = \rho D^2\sqrt{\frac{gD}{2sin\theta}} \qquad \text{-----(1)}$$

$$W_{funnel\ flow} = \frac{\pi D^3 \rho}{4}\sqrt{\frac{2g\delta}{D}} \qquad \text{-----(2)}$$

Only the equation for mass flow shows a dependence of flow rate on hopper inclination angle, which can be linearised to:

$$W_{mass\ flow} = \rho D^2\sqrt{\frac{gD}{2}}sin^{-\frac{1}{2}}\theta$$

For steep hopper angles, mass flow predominates and Equation (1) closely approximates flow rate. However, when hopper inclination becomes gradual and particle movement transitions to mostly funnel flow, Equation (2) will be an estimate of flow rate. At this point, since the formation of arches for funnel flow is independent of hopper inclination angle, the flow rate will remain constant as hopper inclination angle increases.

From the graphing of Equations (1) and (2), it is then hypothesised that at small angles of inclination, flow rate is very high as mass flow predominates but quickly falls as angle of inclination increases and transition to funnel flow occurs. At large angles of inclination, flow rate approaches a constant value.

4.1 Variables, Apparatus, and Methodology

4.1.1 Variables

The independent variable of this investigation is the angle of inclination of the walls of a wedge-shaped hopper. As elaborated in the methodology section, nine hoppers of varying hopper angles from $10°$ to $90°$ were designed.

The dependent variable is the flow rate of sand discharged from the hopper, measured by video analysis with Loggerpro software, recorded with a camera at 240 frames per second.

Controlled Variable	Method of Control	Justification for Control
Type of sand used	The 0.5 mm uniform graded sand used for all the trials were from the same bag.	Ensuring a fair degree of uniformity in size and properties across most of the particles minimises unanticipated variations in interactions between particles of different characteristics.
Material of hopper	All nine hoppers were printed from the same material,	Hopper material significantly affects the coefficient of

Controlled Variable	Method of Control	Justification for Control
	polylactic acid.	kinetic friction between the hopper walls and the particles, thereby affecting the wall friction angle and therefore critical angle of transition between mass and funnel flow.
Hopper aperture size	A square aperture of 10 by 10 mm was printed for all the hoppers.	As hopper aperture size increases, the time taken for sand to discharge decreases.
Environmental conditions: temperature, humidity	All trials were conducted at the same location on the same day, in an enclosed room.	The local temperature and humidity affect the moisture content of the sand, also affecting its wall friction angle.

Figure 6: Table of Controlled Variables

4.1.2 Apparatus

- Hoppers of hopper angles: $10°, 20°, 30°, 40°, 50°, 60°, 70°, 80°, 90°$
- Ender-3 Pro 3D printer
- Polylactic acid filament
- Retort stand with clamps
- 0.5 mm sand
- Mobile phone camera
- Tripod camera stand
- Loggerpro software
- Electronic balance

4.2 Methodology

4.2.1 Hopper design

All the hoppers were designed in the computer-aided designing software, Autodesk Fusion 360. Measurements are presented in millimetres and degrees as is convention in 3D printing, but were converted to metres and radians for calculations.

To ensure uniformity in aperture size, all the hoppers had square apertures of 10 mm length. The height of the sloped portion of the hoppers was also maintained at a constant 10 mm. Since the hoppers were wedge-shaped, their profiles were uniform across the third axis (the y-direction), as seen in Figure 7 (Page 15) depicting the hopper with $60°$ hopper angle. Based on the principles of the Janssen effect (Thorens, 2021), the time taken for granular material to discharge from a hopper is independent of hopper height. Therefore, the heights of each hopper were varied slightly; to accommodate a sufficient amount of sand, the narrower hoppers (of smaller hopper angles) were made taller.

A triangular infill pattern of 20% was used to allow for stability, ensuring that the hopper would be able to support the sand it contained. The width of the walls was 2 mm, and the layer height was 0.2 mm. After the modelling stage in Fusion 360, UltiMaker Cura was used to slice the meshed stl files for printing with an Ender-3 Pro 3D printer.

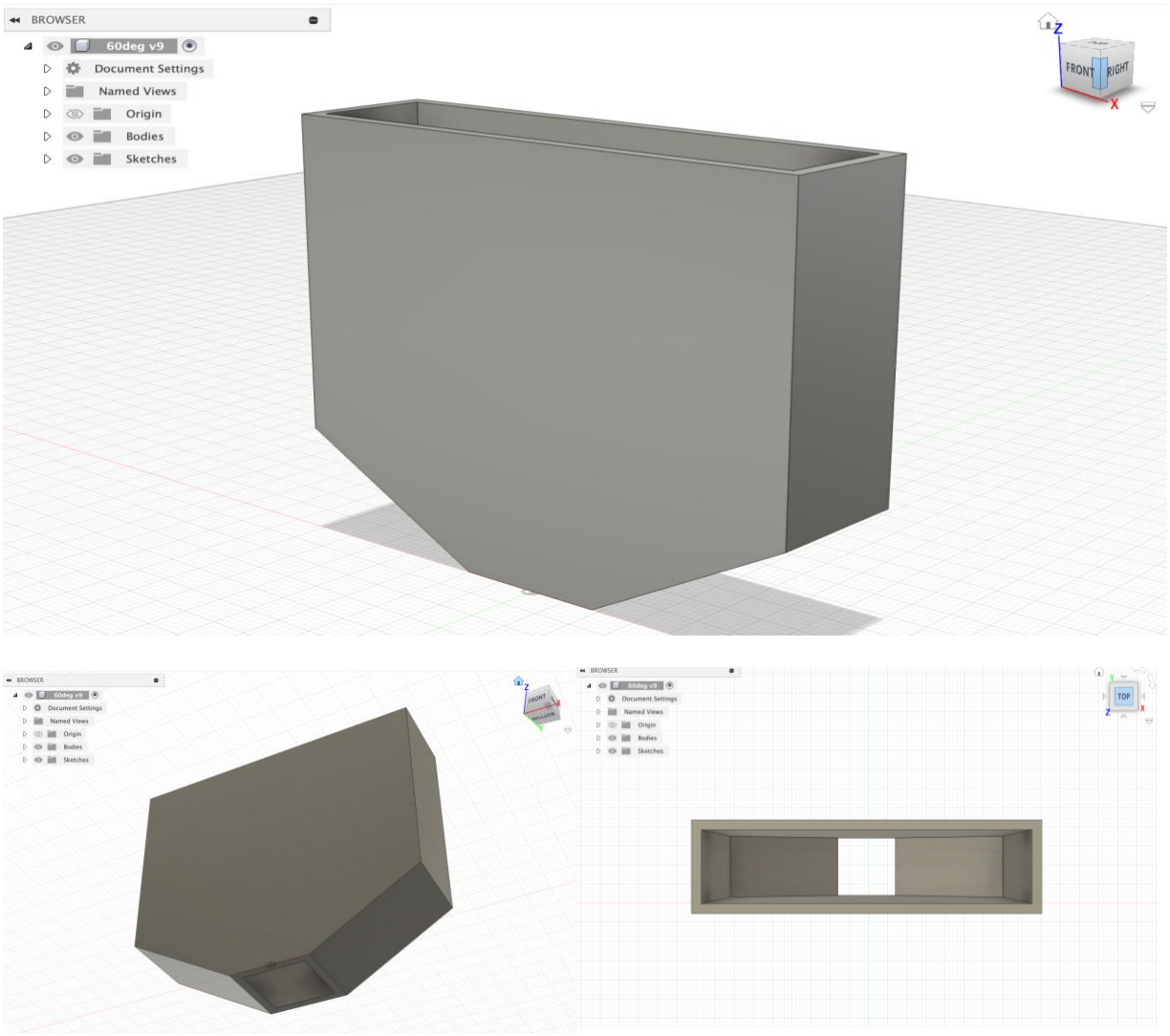

Figure 7: 3D Model of hopper as viewed in Fusion 360

4.2.2 Initial Experimental Design and Preliminary Trials

Initially, the hoppers were constructed out of thin wooden boards. However, human error was high and the cutting of dimensions was imprecise. Additionally, the pieces were difficult to glue together and bent out of place. Hence, this strategy was forsaken in favour of 3D printing. With the printer's high degree of precision and the utility of computer-aided design, and the structural stability of printed materials, the 3D printed hoppers were far more suitable.

A retort stand was set up next to the camera tripod such that each hopper was held by a clamp with its aperture at eye level with the camera. A white Styrofoam board was set up behind the retort stand to contrast with the dark-coloured sand, making the sand particles easier to identify during video analysis. A tray was set up below the hopper to collect the discharged sand.

During preliminary trials, it was observed that at greater hopper angles, stagnation areas formed readily and a significant amount of sand was left stuck within the hopper. This is illustrated in Figure 8, a photograph of the 80° hopper where the stagnation areas are clearly seen through the translucent material. The dark silhouettes on either side of the aperture as labelled demarcate the piles of sand stuck within the hopper, even after flow has stopped.

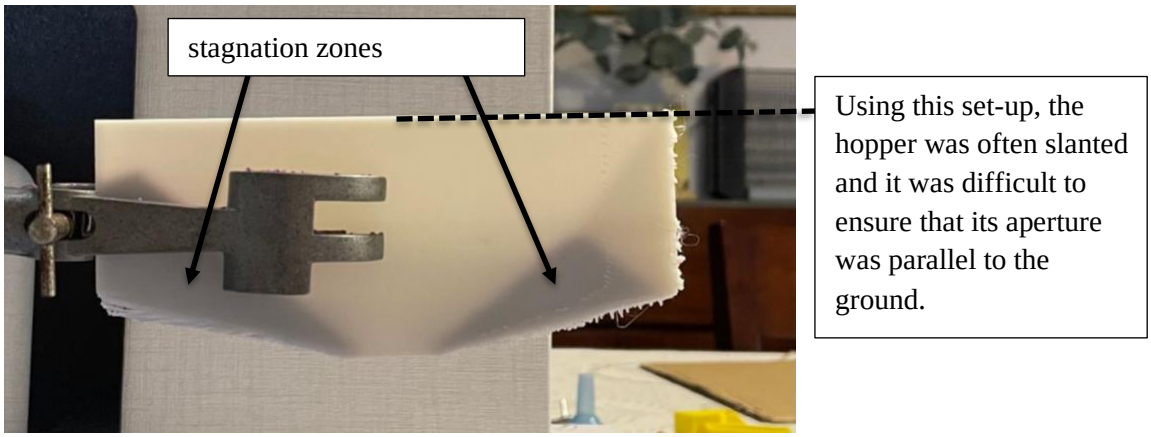

Figure 8: Stagnation zones formed during preliminary trials

Thus, it was not possible to simply measure the time taken for sand to finish flowing through the hopper. Video analysis was used to measure the time taken for sand to stop flowing, and the sand that had been discharged was collected. Since it has been found that flow rate is constant (Mehdizad, 2021), the flow rate was then calculated based on the time taken for the measured mass of sand to flow through the hopper.

Additionally, the initial strategy of using the retort stand clamps to directly support the hopper was impractical. It was difficult to align the hopper with the aperture parallel to the table, as seen in Figure 8 (Page 16) where the hopper was slightly slanted.

4.2.3 Final Experimental Design and Procedure

In order to ensure the hopper could be levelled such that the sand could symmetrically flow through, the set-up was revised in a way that provided more support for the hopper, seen in Figure 9. A thick piece of cupboard, capable of supporting the weight of the hopper and sand was acquired and a hole slightly bigger than the size of the hopper aperture was cut in the cupboard. The outer walls of the hopper were then attached to the cupboard base with blue-tack adhesive and the cupboard base was held up by a pair of retort stands. To ensure the hopper was level, another piece of cupboard was placed over the top of the hopper and a circular bubble level was placed on top. The clamps of the retort stand were then adjusted to and appropriate heights to keep the hopper level.

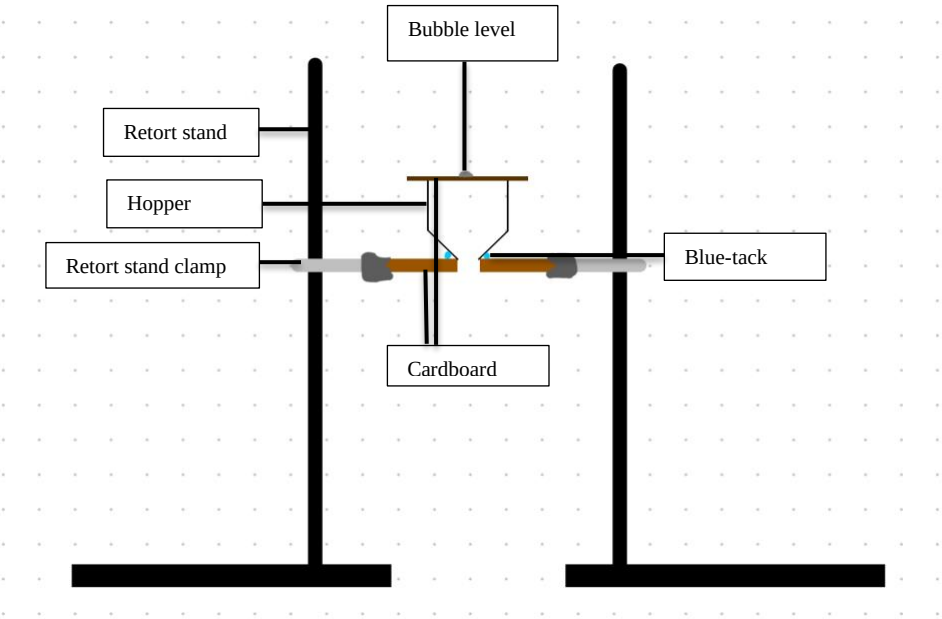

Figure 9: Schematic of final experimental set-up

100 grams of sand was measured using an electronic scale and added into the hopper, covering the hopper's bottom aperture with a small cardboard strip while filling. Video recording was started and the cardboard strip was quickly removed. Video recording was stopped when sand stopped flowing. The mass of the sand collected at the end of each experiment was measured using the electronic scale and recorded.

The recorded videos were imported into the Loggerpro video analysis software, and a frame-by-frame analysis was carried out to pinpoint the exact frame in which the first and last grains of sand flow through the hopper. From the timestamps provided, the time difference between these two events were recorded as the time taken for the given amount of sand to flow through the hopper.

5.1 Data and Analysis

5.1 Tables of Raw and Processed Data

Table of Raw Data

θ /rad	$\Delta\theta$ /rad	Trial 1		Trial 2		Trial 3		Trial 4		Trial 5	
		m /kg (±0.0001 kg)	t /s (±0.001s)	m /kg (±0.0001 kg)	t /s (±0.001s)	m /kg (±0.0001 kg)	t /s (±0.001s)	m /kg (±0.0001 kg)	t /s (±0.001s)	m /kg (±0.0001 kg)	t /s (±0.001s)
0.175	0.009	0.1000	1.2701	0.1000	1.2535	0.1000	1.2592	0.1000	1.2652	0.1000	1.2525
0.35	0.01	0.1000	1.7629	0.1000	1.7629	0.1000	1.7936	0.1000	1.7715	0.1000	1.7733
0.52	0.01	0.1000	2.2503	0.1000	2.2103	0.1000	2.2310	0.1000	2.2652	0.1000	2.2518

θ /rad	$\Delta\theta$ /rad	Trial 1		Trial 2		Trial 3		Trial 4		Trial 5	
		m /kg (±0.0001 kg)	t /s (±0.001s)	m /kg (±0.0001 kg)	t /s (±0.001s)	m /kg (±0.0001 kg)	t /s (±0.001s)	m /kg (±0.0001 kg)	t /s (±0.001s)	m /kg (±0.0001 kg)	t /s (±0.001s)
0.70	0.01	0.1000	2.4169	0.1000	2.4701	0.1000	2.4533	0.0982	2.4018	0.1000	2.4722
0.873	0.009	0.0937	2.4664	0.0892	2.3628	0.0962	2.5465	0.0921	2.4357	0.0904	2.4364
1.047	0.007	0.0883	2.3613	0.0837	2.1768	0.0852	2.2569	0.0810	2.1750	0.0844	2.2580
1.222	0.005	0.0849	2.2080	0.0824	2.2066	0.0874	2.3289	0.0821	2.2074	0.0818	2.1669
1.396	0.004	0.0723	1.9512	0.0793	2.1318	0.0729	1.9031	0.0742	1.9699	0.0702	1.8601
1.571	0.003	0.0634	1.6884	0.0621	1.6716	0.0640	1.6899	0.0639	1.6831	0.0627	1.6720

Figure 10: Table of Raw Data

Table of Processed Data

θ /rad	$\Delta\theta$ /rad	Flow rate, W/kgs^{-1}					W_{ave} / kgs^{-1}	ΔW_{ave} / kgs^{-1}
		W_1	W_2	W_3	W_4	W_5		
0.175	0.009	0.079	0.080	0.079	0.079	0.080	0.079	0.001
0.35	0.01	0.057	0.057	0.056	0.056	0.056	0.056	0.001
0.52	0.01	0.044	0.045	0.045	0.044	0.044	0.045	0.001
0.70	0.01	0.0414	0.0405	0.0408	0.0409	0.0405	0.0408	0.0009

θ /rad	$\Delta\theta$ /rad	Flow rate, W/kgs^{-1}					W_{ave} / kgs^{-1}	ΔW_{ave} / kgs^{-1}
		W_1	W_2	W_3	W_4	W_5		
0.873	0.009	0.038	0.0378	0.0378	0.0378	0.0371	0.0377	0.0009
1.047	0.007	0.0374	0.0382	0.0378	0.0372	0.0374	0.0376	0.0009
1.222	0.005	0.038	0.037	0.038	0.037	0.038	0.038	0.001
1.396	0.004	0.037	0.037	0.038	0.038	0.038	0.038	0.001
1.571	0.003	0.0376	0.0372	0.0379	0.038	0.0375	0.0376	0.0008

Figure 11: Table of Processed Data

Using values from the first trial of the 0.175 rad hopper for sample derivations,

Formula	Sample Derivation
$W = \frac{mass\ of\ sand\ collected}{time\ taken\ for\ discharge}$	$W = \frac{0.1}{1.27008}$ $= 0.078735\ kgs^{-1}\ (5\ sf)$
$W_{ave} = \frac{W_1+W_2+W_3+W_4+W_5}{5}$	$W_{ave} = \frac{0.078735+0.079778+0.079418+0.079038+0.079840}{5}$ $= 0.079362\ kgs^{-1}\ (5sf)$ $= 0.079\ kgs^{-1}\ (3dp)$
$\Delta W_{ave} = \frac{W_{max}-W_{min}}{2}$	$\Delta W_{ave} = \frac{0.079840-0.078735}{2}$ $= 0.001\ kgs^{-1}\ (1sf)$

Figure 12: Error Propagation and Sample Derivation

To determine the uncertainty of the hopper angle, θ, the geometry of the design as well as 3D printer specifications must be referenced. The Ender-3 Pro 3D Printer has a precision of 0.1mm, and the layer height used was 0.2mm to ensure stability. The sloped portion of the hopper, *y*, was kept at a constant $15\ (\pm 0.1)$ mm for all the hoppers.

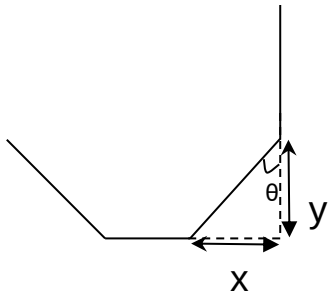

Figure 13: Definition of parameters

θ /rad	*x* /mm (±0.1 mm)
0.175	2.6
0.35	5.5
0.52	8.7
0.70	12.6
0.873	17.9
1.047	26.0
1.222	41.2
1.396	60.1
1.571	10.0

Figure 14: Derivation of uncertainty in angle

θ is given by $arctan(\frac{x}{y})$. Taking the partial derivative of $arctan(\frac{x}{y})$ with respect to *x* gives the uncertainty of θ with as a result of the uncertainty of *x*:

$$\frac{\delta}{\delta x}\arctan\left(\frac{x}{y}\right) = \frac{y}{x^2 + y^2}$$

Repeating the process with respect to *y*, then adding the values obtained to give the uncertainty of θ:

$$\Delta\theta = (\frac{y}{x^2+y^2})(\Delta x) + (\frac{x}{x^2+y^2})(\Delta y)$$

Sample Derivation

$\Delta\theta$	Sample Derivation
$\Delta\theta = (\frac{y}{x^2+y^2})(\Delta x) + (\frac{x}{x^2+y^2})(\Delta y)$	$\Delta\theta = (\frac{15}{2.645^2+15^2})(\Delta 0.1) + (\frac{2.645}{2.645^2+15^2})(\Delta 0.2)$ $=0.009$

Figure 15: Sample derivation for angle

θ /rad	$\Delta\theta$ /rad	W_{ave} /kgs^{-1}	ΔW_{ave} /kgs^{-1}
0.175	0.009	0.079	0.001
0.35	0.01	0.056	0.001
0.52	0.01	0.045	0.001
0.70	0.01	0.0408	0.0009
0.873	0.009	0.0377	0.0009
1.047	0.007	0.0376	0.0009
1.222	0.005	0.038	0.001
1.396	0.004	0.038	0.001
1.571	0.003	0.0376	0.0008

Figure 16: Table of data with uncertainties

Value	Uncertainty Calculations
$W_{funnel\ ave} = \frac{W_{f1} + W_{f2} + W_{f3} + W_{f4}}{4}$ $W_{funnel\ ave} = \frac{0.0376 + 0.038 + 0.0376 + 0.038}{4}$ $= 0.0378\ kgs^{-1}\ (4dp)$	$\Delta W_{funnel\ ave} = \frac{W_{funnel\ max} - W_{funnel\ min}}{2}$ $= \frac{0.038 - 0.0376}{2}$ $= 0.0002\ kgs^{-1}\ (1sf)$

Figure 17: Calculation of funnel flow rate

For hopper angles greater than 0.873 rad, flow rate approaches a constant, as predicted. The average of the final four values of hopper angles 1.047 to 1.571 rad is calculated in Figure 17 to be:

$$W_{funnel\ flow} = 0.0378 \pm 0.0002$$

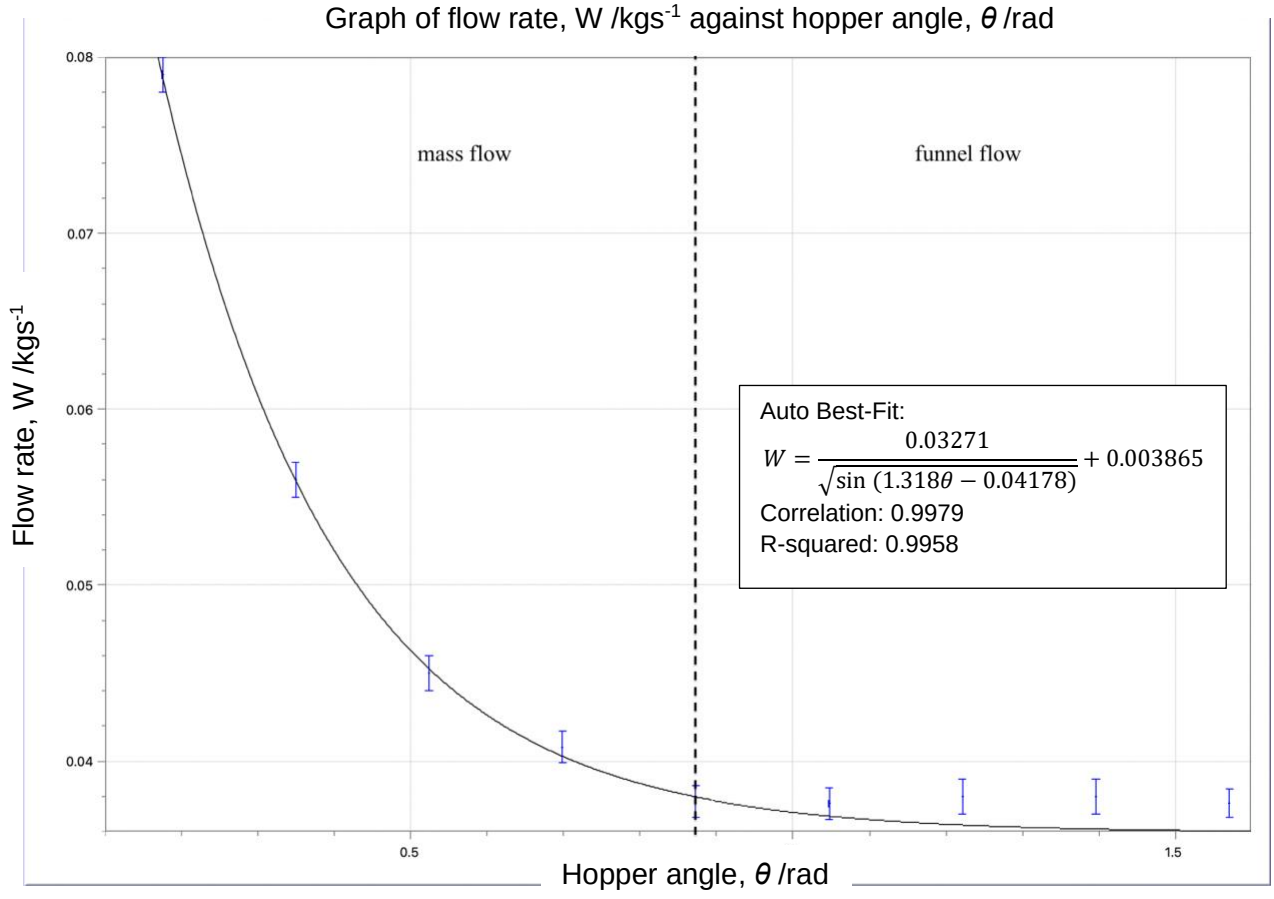

Figure 18: Graph of flow rate, W /kgs^{-1} against hopper angle, θ /rad

5.2 Analysis

From Figure 18 (Page 23), as hopper angle increases for small angles, flow rate rapidly decreases. The software-generated line of best-fit in accordance with the predicted inverse root sine form gives a high R-squared value of 0.9958, suggesting a very good fit for angles equal to or smaller than 0.873 rad. After 0.873 rad, the inverse root sine trend no longer passes through successive points and the relationship no longer holds.

For larger hopper angles, flow rate approaches a constant value of about $0.0378\ kgs^{-1}$ from 0.873 to 1.571 rad:

$$\frac{\pi D^3 \rho}{4}\sqrt{\frac{2g\delta}{D}} = 0.0378 \pm 0.0002$$

For the smaller hopper angles from 0.175 to 0.873 rad, flow rate decreases rapidly from 0.079 to 0.0377, at a decreasing rate. From an inspection of Figure 18 (Page 23), the data appears to support the hypothesis of flow rate following an inverse root sine trend. To confirm this, for the aforementioned domain, a linearised plot is shown of W_{ave} (kgs^{-1}) against $sin^{-\frac{1}{2}}\theta$.

W_{ave} /kgs^{-1}	ΔW_{ave} /kgs^{-1}	$sin^{-\frac{1}{2}}\theta$	$\Delta sin^{-\frac{1}{2}}\theta$
0.079	0.001	2.40	0.06
0.056	0.001	1.71	0.02
0.045	0.001	1.41	0.01

W_{ave} /kgs^{-1}	ΔW_{ave} /kgs^{-1}	$sin^{-\frac{1}{2}}\theta$	$\Delta sin^{-\frac{1}{2}}\theta$
0.0408	0.0009	1.247	0.007
0.0377	0.0009	1.143	0.004

Figure 19: Table of linearised data

Error Propagation

Formula	Sample Derivation
$\left\|\frac{d}{d\theta}(sin^{-\frac{1}{2}}\theta)\right\| = \frac{cos\theta}{2sin^{\frac{3}{2}}\theta}$ $d(sin^{-\frac{1}{2}}\theta) = (\frac{cos\theta}{2sin^{\frac{3}{2}}\theta})(d\theta)$	$\Delta sin^{-\frac{1}{2}}(\frac{\pi}{18}) = (\frac{cos\frac{\pi}{18}}{2sin^{\frac{3}{2}}\frac{\pi}{18}})(0.009)$ $= 0.061243\ (5sf)$ $= 0.06\ (1sf)$

Figure 20: Error propagation of linearised data

Graph of W /kgs^{-1} against $sin^{-\frac{1}{2}}\theta$

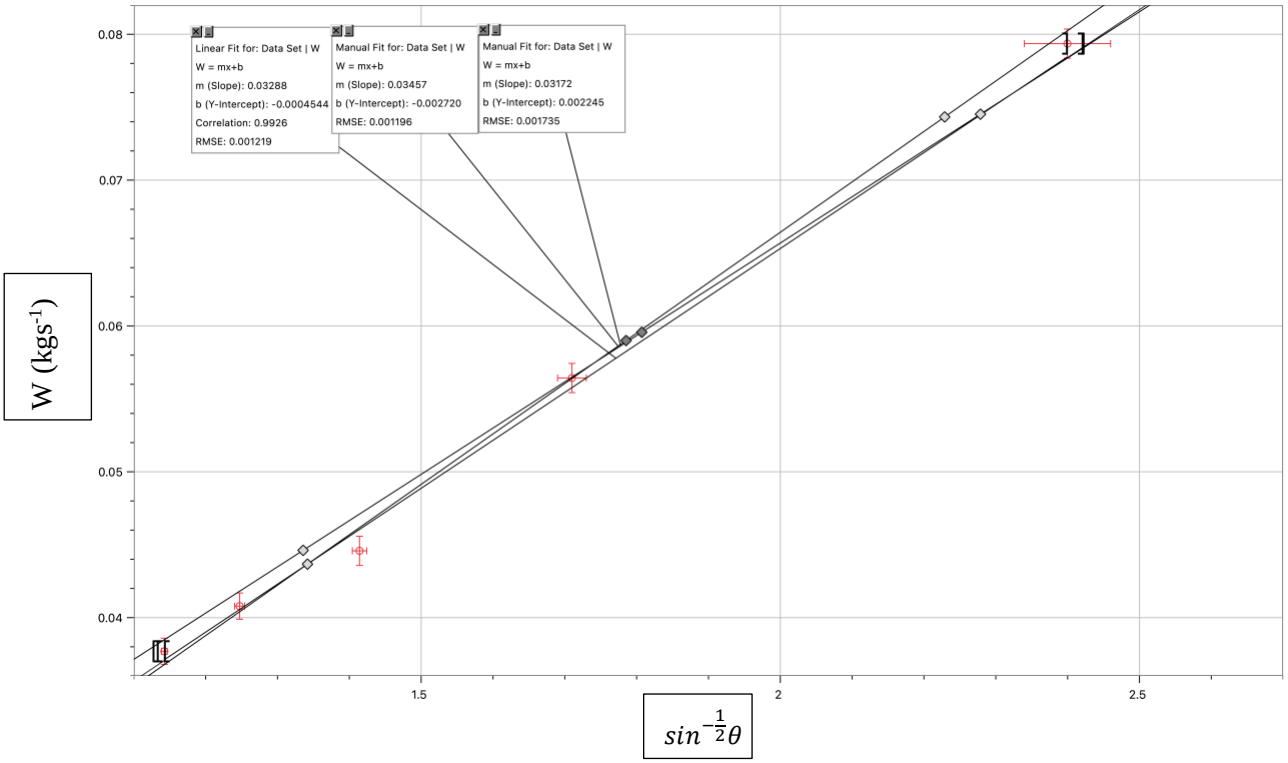

Figure 21: Graph of W /kgs^{-1} against $sin^{-\frac{1}{2}}\theta$

Value	Uncertainty Calculations
$gradient = 0.03361\ (4sf)$ $= 0.034\ (3dp)$	$gradient\ uncertainty = \frac{gradient_{max} - gradient_{min}}{2}$ $= \frac{0.03457 - 0.03172}{2}$ $= 0.001\ (1sf)$ $percentage\ uncertainty = \left(\frac{0.001}{0.034}\right)(100\%)$ $= 2.9\%\ (2sf)$
$y - intercept$ $= -0.0004544\ (4sf)$ $= 0.000\ (3dp)$	$y - intercept\ uncertainty = \frac{intercept_{max} - intercept_{min}}{2}$ $= \frac{0.002245 - (-0.002720)}{2}$ $= 0.002\ (1sf)$

Figure 22: Calculation of percentage uncertainty of gradient

From Figure 21 (Page 25), W is linearly related to $sin^{-\frac{1}{2}}\theta$. The plot has a high correlation of 0.9978, showing the strong adherence to the linear relationship as predicted:

$$W = (0.034 \pm 0.001)sin^{-\frac{1}{2}}\theta + (0 \pm 0.002)$$

wherein the gradient is given by:

$$\rho D^2\sqrt{\frac{gD}{2}} = 0.034 \pm 0.001$$

The value of the gradient given allows for a calculation of the bulk density of the garden sand used to be approximately 1500 kgm^{-3}, which fits within the typical range of sand (Leinov et al.,

2015), confirming the validity of the relationship. The y-intercept is of no physical significance as $sin^{-\frac{1}{2}}\theta \geq 1$ for all values of θ.

5.3 Discussion and Conclusion

The research questioned addressed in this investigation is: **how does hopper angle affect the flow rate of sand through a wedge-shaped hopper with a square aperture?** It was hypothesised that flow rate rapidly decreases as hopper angle increases before plateauing at larger hopper angles. The results obtained confirm the hypothesis that Equations (1) and (2) are obeyed at small and large hopper angles respectively:

$$W_{mass\ flow} = (0.034 \pm 0.001)sin^{-\frac{1}{2}}\theta + (0 \pm 0.002)$$

$$W_{funnel\ flow} = 0.0378 \pm 0.0002$$

For smaller hopper angles from 0.175 to 0.873 rad, the dependence of flow rate on hopper angle indicates the predominance of mass flow; particles are able to flow along without getting stuck in stagnation areas, meaning that the primary resistive force acting on each particle is the friction between the particle and the hopper walls, rather than the friction between moving and stationary particles. While mass flow prevails, as the hopper angle increases, the vertical component of the normal contact force exerted on each particle of sand by the slanted hopper walls increases. This causes a decrease in the net downward force accelerating each particle toward the hopper aperture, leading to each particle leaving the aperture at a slower speed on average, causing a decrease in flow rate.

As hopper angle increases past 0.873 rad, the flow pattern transitions from mass to funnel flow. Particle flow is no longer reliant on hopper angle as stagnation zones formed from accumulated stationary particles become so prevalent that particles flow out of the hopper only after the collapse of momentarily formed arches (Oldal, 2011). As such, the speed at which particles exit

the hopper is only affected by the height of these arches. Graphically, this transition occurs at a hopper angle of about 0.873 rad, which corroborates with the literature-accepted critical angle of 55° (Anand et al., 2008, Tangri et al., 2019). From this angle onwards, the flow rate tends towards a constant value of about 0.0378 kgs^{-1}.

This trend is supported by other works. Oldal (2011), confirms the relationship hypothesised and compares the experimental data with the Beverloo and Johanson equations, concluding a strong corroboration in the funnel flow region. Due to the inability of the empirically determined Beverloo and Johanson equations to account for a specific relationship between hopper angle and flow rate, no comparison can be made for the mass flow relationship. Although all three models are capable of accurately describing discharge rate, the advantage of the theoretically derived relationship is its ability to ascribe physical significance to its parameters, more effectively conveying the factors influencing discharge rate. Camila (2018) also finds a similar relationship in the transition between mass and funnel flow, noting that the lower critical angle found was a result of using non-uniform grains.

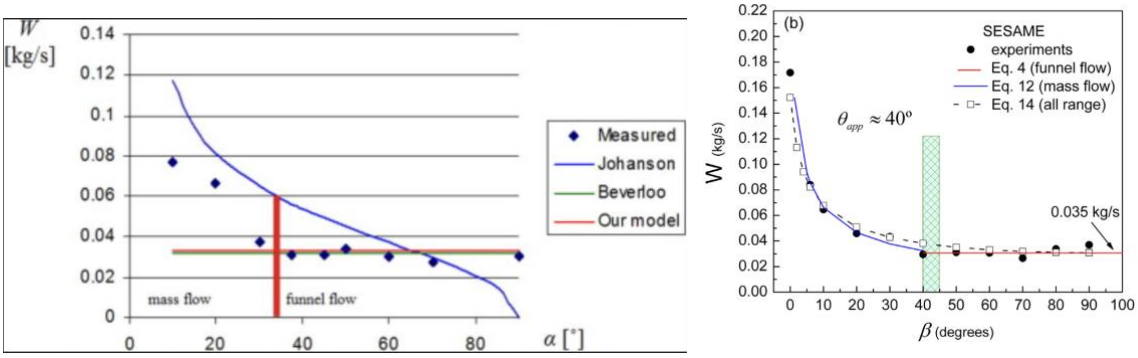

Figure 23: Experimental results from Oldal (2011) (left) and Camila (2018) (right)

6.1 Evaluation

One of the strengths of this investigation was the use of 3D printing and computer-aided design for the preparation of hoppers. This has allowed for the hopper geometry to be precisely

controlled, giving rise to very little uncertainty in hopper angle. In Figure 18 (Page 23), horizontal error bars for angle have been included but they are so small that they cannot be seen at a reasonable scale. Additionally, the small vertical error bars in Figure 21 (Page 25) and the small percentage uncertainty in the gradient of 2.9% also indicate that the results were subject to a very small degree of random error. This could be attributed to the fact that the experiments were carried out on the same day at the same location, allowing for minimal variation in environmental conditions.

Another strength was that the slow-motion camera had a high frame rate. As compared to other methods of measuring time taken, such as with a stopwatch, human error is greatly reduced by using video analysis to determine the exact frame at which a grain exits the hopper. Due to the miniscule size of each individual grain, judgement of the grains' position is difficult, especially in real-time. Furthermore, using slow-motion video analysis allows the time measurement to be no longer subject to delayed human reaction time that would otherwise immensely affect readings.

However, a limitation of this study was the inability to ensure the exact uniformity of the sand grains. Mankoc (2008) found that jamming was a particularly prevalent phenomenon in non-uniform grains, especially on the small scale. Thus, although the relative size of each grain to the aperture was relatively small, random error could have arisen from certain orientations of sand grains inadvertently causing jamming to occur, randomly lowering discharge rate.

6.2 Applications and Future Extensions

This investigation has confirmed the rapid rate at which flow rate decreases with hopper angle. Industrial applications often aim to maximise flow rate to accelerate the production process, implying that the hopper angle should be as small as possible. However, hoppers of small angles require a much longer height to accommodate the same volume of material, making them

impractical due to space constraints. Results indicate that the transition from mass to funnel flow occurs at hopper angles of around 50°; this is the upper limit that hopper designers should fall below to ensure the predominance of mass flow.

An extension for future work could involve the scalability of studied relationships between hopper geometry and discharge rate. Most experimental studies involving hopper geometry are necessarily on a small scale. However, it has been noted that certain models fail when aperture size changes beyond a certain range. Given the wide applications of larger-scaled hoppers in industry, it would be crucial to test the validity of theoretical relationships on larger hoppers.

References

Anand, A. S., Curtis, J. S., Wassgren, C., Hancock, B. C., & Ketterhagen, W. R. (2008). *Predicting discharge dynamics from a rectangular hopper using the discrete element method (DEM)*. *63*(24), 5821–5830. https://doi.org/10.1016/j.ces.2008.08.015

Beverloo, W. A., Leniger, H. A., & van de Velde, J. (1961). The flow of granular solids through orifices. *Chemical Engineering Science*, *15*(3), 260–269. https://doi.org/10.1016/0009-2509(61)85030-6

Camila, M., Jesica Gisele Benito, Rodolfo Omar Uñac, & Ana Maria Vidales. (2018). Towards a one parameter equation for a silo discharging model with inclined outlets. *Powder Technology*, *336*, 265–272. https://doi.org/10.1016/j.powtec.2018.06.010

Guo, C., Ye, K., Xu, Y., Dai, X., Zheng, J., & Ya, M. (2023). Discharge characteristics of conical and hyperbolic hoppers based on discharge time distribution. *Powder Technology*, *426*, 118665–118665. https://doi.org/10.1016/j.powtec.2023.118665

Huang, X., Zheng, Q., Liu, D., Yu, A., & Yan, W. (2022). A design method of hopper shape optimization with improved mass flow pattern and reduced particle segregation. *Chemical Engineering Science*, *253*, 117579. https://doi.org/10.1016/j.ces.2022.117579

Janssen, H. A. (1895). Versuche uber Getreidedruck in Silozellen. *Verein Deutscher Ingenieure*, *39*(35), 1045–1049.

Jenike, A. W. (1964). Storage and Flow of Solids. *Bulletin of the University of Utah*, *53*(26).

José Ramón Darias, Marcos Andrés Madrid, & Luis Ariel Pugnaloni. (2020). Differential equation for the flow rate of discharging silos based on energy balance. *Physical Review*, *101*(5). https://doi.org/10.1103/physreve.101.052905

Leinov, E., Lowe, M. R., & Cawley, P. (2015). *Investigation of guided wave propagation and attenuation in pipe buried in sand*. *347*, 96–114. https://doi.org/10.1016/j.jsv.2015.02.036

Mankoc, C., Janda, A., Arévalo, R., Pastor, J. M., Zuriguel, I., Garcimartín, A., & Maza, D. (2008). The flow rate of granular materials through an orifice. *Granular Matter*, *10*(6), 469–469. https://doi.org/10.1007/s10035-008-0114-2

Maraveas, C. (2020). Concrete Silos: Failures, Design Issues and Repair/Strengthening Methods. *Applied Sciences*, *10*(11), 3938. https://doi.org/10.3390/app10113938

Mehdizad, M., Fullard, L., Galvosas, P., & Holland, D. (2021). Quantitative measurements of flow dynamics in 3D hoppers using MRI. *Powder Technology*, *392*, 69–80. https://doi.org/10.1016/j.powtec.2021.06.048

Mellmann, J., Hoffmann, T., & Fürll, C. (2014). Mass flow during unloading of agricultural bulk materials from silos depending on particle form, flow properties and geometry of the discharge opening. *Powder Technology*, *253*, 46–52. https://doi.org/10.1016/j.powtec.2013.11.010

Nedderman, R. M., Ugur Tüzün, Savage, S. B., & Houlsby, G. T. (1982). The flow of granular materials—I. *Chemical Engineering Science*, *37*(11), 1597–1609. https://doi.org/10.1016/0009-2509(82)80029-8

Oldal, I., Keppler, I., Csizmadia, B., & Fenyvesi, L. (2012). Outflow properties of silos: The effect of arching. *Advanced Powder Technology*, *23*(3), 290–297. https://doi.org/10.1016/j.apt.2011.03.013

Tang, Y., Chan, D. H., & Zhu, D. Z. (2022). The modeling of free-fall arch formation in granular flow through an aperture. *Frontiers in Physics*, *10*. https://doi.org/10.3389/fphy.2022.963495

Tangri, H., Guo, Y., & Curtis, J. S. (2019). Hopper discharge of elongated particles of varying aspect ratio: Experiments and DEM simulations. *Chemical Engineering Science: X*, *4*, 100040. https://doi.org/10.1016/j.cesx.2019.100040

Thorens, L., Måløy, K. J., Bourgoin, M., & Santucci, S. (2021). Magnetic Janssen effect. *Nature Communications*, *12*(1). https://doi.org/10.1038/s41467-021-22722-y

Uñac, R. O., Vidales, A. M., Benegas, O. A., & Ippolito, I. (2012). Experimental study of discharge rate fluctuations in a silo with different hopper geometries. *Powder Technology*, *225*, 214–220. https://doi.org/10.1016/j.powtec.2012.04.013

Verghese, T. M., & Nedderman, R. M. (1995). The discharge of fine sands from conical hoppers. *Chemical Engineering Science*, *50*(19), 3143–3153. https://doi.org/10.1016/0009-2509(95)00165-2

Vladimir Valerievich Ivchenko. (2023). Beyond Stevin's law: the Janssen effect. *European Journal of Physics*, *44*(2), 025006–025006. https://doi.org/10.1088/1361-6404/acb470

Wiącek, J., Horabik, J., Molenda, M., Parafiniuk, P., Bańda, M., & Stasiak, M. (2023). Converging orifice used to control the discharge rate of spherical particles from a

flat floor silo. *Scientific Reports*, *13*(1), 669. https://doi.org/10.1038/s41598-023-27431-8

Zhi Hong Gu. (1991). *Gravity flowrate of bulk solids from mass flow bins*.